Engineering Failure Analysis 112 (2020) 104517

Contents lists available at ScienceDirect

Engineering Failure Analysis

journal homepage: www.elsevier.com/locate/engfailanal

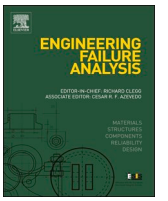

Digital twin based condition monitoring of a knuckle boom crane: An experimental study

Torbjørn Moi*, Andrej Cibicik, Terje Rølvåg

Department of Mechanical and Industrial Engineering, Norwegian University of Science and Technology (NTNU), NO-7491 Trondheim, Norway

ARTICLE INFO

Keywords:
Cranes
Fatigue data
Finite element analysis
Load history
Strain gauging

ABSTRACT

This paper presents a novel approach for implementation of a digital twin for condition monitoring of a small-scale knuckle boom crane. The digital twin of the crane is simulated real-time in a nonlinear finite element (FE) program, where the estimated payload weight is used as an input. We implement an inverse method for estimation of the weight as well as its force vector direction based on physical strain gauge measurements. Additional strain gauges were utilized for validation of accuracy of the digital twin and inverse method. Based on a few physical sensor outputs, the digital twin allows for real-time determination of stresses, strains and loads at an unlimited number of hot spots. Therefore a digital twin can be an effective tool for predictive maintenance and product life-cycle management. In addition, condition monitoring of cranes during heavy-lift operations increases safety and reliability.

The presented approach is described in a general manner and is applicable for various robotic manipulators used in the industry.

1. Introduction

Cranes are indispensable in many industrial operations. Offshore cranes are both used for installation operations and are an important part of supply chains of offshore installations. Cranes operate in demanding environmental conditions and are subjected to dynamic wave loads. In addition, cranes are often used for heavy-lift operations. When a crane operates, its configuration changes, which makes it even more difficult to determine the effect of the load combination on various components of the crane. Application of digital twins for condition monitoring, predictive maintenance and life-cycle management can be a reasonable solution, as, based on data from only few sensors, it provides real-time stresses in the entire structure and loads in the components such as bearings, shafts, cables, hydraulic cylinders, etc. Such data can be recorded and stored throughout the life-time of the machine. This is a cost-efficient solution since no additional physical instrumentation is needed.

In general, digital twin is a term used to describe a model or several models of a physical structure, mechanism, process or system, where each model is specifically derived for collection and generation of relevant data [1–3]. The model should also accurately describe properties and behavior of a physical system, such that the data obtained from the model is reliable. The concept of a digital twin for a mechanical system was demonstrated by a simple example of a fixed beam in bending in [1], where the CAD (Computer-Aided Design) model of the beam and stress analysis tools were used in combination with sensors attached to the beam. The authors suggested that the next step of the research was to implement the concept for a moving mechanism. Some research on implementation of digital twins for mechanisms is already available. An interesting case of a digital twin for a helicopter rotor system

* Corresponding author.
E-mail addresses: tobbmoi@gmail.com (T. Moi), andrej.cibicik@ntnu.no (A. Cibicik), terje.rolvag@ntnu.no (T. Rølvåg).

https://doi.org/10.1016/j.engfailanal.2020.104517
Received 24 October 2019; Received in revised form 3 March 2020; Accepted 25 March 2020
Available online 27 March 2020
1350-6307/

was presented in [4], where the loads and displacements at the joints of the mechanism were calculated based on sensor data and dynamic multibody simulation. The authors suggested that knowledge of exact loads applied on mechanical components in real operation would improve prediction of maintenance. Some other examples of application of digital twins for condition monitoring and predictive maintenance within aerospace industry were given in [5–7]. In addition to digital twins of mechanisms in operation, similar concepts and experimental studies can be found for manufacturing machines and tools. For example, digital twins for CNC machines were discussed in [8–11]. Importance of digital twins for autonomous systems in manufacturing was discussed in [12]. A review of scientific literature reveals that many methods for implementation of digital twins for mechanisms, like cranes, can be applicable for autonomous systems used in manufacturing. This is especially relevant for robotic manipulator arms used in manufacturing, since a crane is mechanically very similar to a robotic manipulator. Digital twins for robotic manipulators were discussed in [13–16].

The main contribution of this work is a novel approach for implementation of a digital twin monitoring solution for a knuckle boom crane, which is also applicable for other robotic manipulators used in the industrial processes. This work is an extension of the short conference contribution [17]. The proposed digital twin solution was implemented for the case of a small-scale knuckle boom crane and verified by experiments. The proposed approach can be efficiently used for predictive maintenance and life-cycle management of cranes and their components, by continuously collecting data about motion of a crane and loads a crane and its components are exposed to. In addition, the possibility of real-time data acquisition allows for increasing reliability and reducing risk under heavy-lift operations. Industrial cranes as well as robotic manipulators are often an important part of the manufacturing process, and the proposed solution can be integrated into digital twin of an entire production line, which would contribute to efficiency and optimisation.

2. Preliminaries on inverse methods

A problem in structural dynamics where the response of the structure is found from applied known loads is referred to as a forward problem. An inverse problem for digital twins refers to the process of estimating the excitation the structure is subjected to from physical sensor measurements of the structural response. The method used to do this is referred to as an inverse method.

2.1. The inverse problem

The inverse problem is ill-posed [18]. In a well-posed problem, there is a unique solution to any reasonable measured data. For the inverse problem, this is not necessarily the case. Some problems are:

- The solution does not have to be unique.
- The measured data is most likely incomplete (all deformations are not measured).
- Noise and drifting in the sensor data can lead to undefined solutions.
- The location of the external forces may be unknown.

These problems must be addressed when developing inverse methods. For the case of digital twins of mechanisms like a crane, there are additional requirements for the method:

- It should be able to run continuously with real-time data.
- It should be computationally efficient for real-time calculations of large systems.
- It should be stable over long time periods.
- It should be able to handle large displacements of mechanisms.

Several inverse methods were presented and tested in scientific papers previously, but to the best of knowledge of the authors none satisfy all the requirements listed above. They are too computationally expensive [19–21], are only tested for short time intervals on small systems [18–29], or do not consider measurement noise [23]. In addition, most of the methods are only tested on numerically generated inputs, and none seem to consider mechanisms [18–31].

2.2. Method basis

We propose a novel inverse method to meet the demands of digital twins. It is based on a known equal number of applied forces and strain gauges at known locations and utilizes finite element simulation. Rølvåg et al. [32] described how a virtual strain rosette can be formulated using a zero-stiffness membrane element connected to nodes around the area where strain is to be determined. For this membrane element, there exists an element strain–displacement matrix which gives a vector of strains $\widetilde{\boldsymbol{\varepsilon}}$ as

$$\widetilde{\boldsymbol{\varepsilon}} = \widetilde{\boldsymbol{B}}_e \widetilde{\boldsymbol{v}}_e \tag{1}$$

where $\widetilde{\boldsymbol{B}}_e$ is the strain–displacement matrix of the element, and $\widetilde{\boldsymbol{v}}_e$ is the strain rosette element local displacements. These strains must be transformed into Cartesian coordinates with the transformation matrix $\boldsymbol{T}_r$, and the strains in one direction (leg) of the virtual rosette isolated with $\boldsymbol{t}_l$. Expanding the equation further to relate strains to global displacements $\boldsymbol{v}$, gives

$$\varepsilon_l = [\boldsymbol{t}_l \boldsymbol{T}_{\varepsilon_r} \widetilde{\boldsymbol{B}}_e \boldsymbol{T}_e \boldsymbol{N}_e \boldsymbol{L}]\boldsymbol{v} \tag{2}$$

with $\boldsymbol{N}_e$ being a matrix of ones and zeroes for selecting the strain rosette element displacements. $\boldsymbol{T}_e$ transforms these displacements into the element local coordinate system. Finally, $\boldsymbol{L}$ expands the system to include linearly constrained displacements. This means that strains are linearly related to the displacements of the systems, where it is assumed that the matrices in Eq. (2) are constant.

In a linear static system, the displacements are linearly related to the external load $\boldsymbol{Q}$ by the stiffness matrix $\boldsymbol{K}$

$$\boldsymbol{K}\boldsymbol{v} = \boldsymbol{Q}. \tag{3}$$

Assuming that only applied forces $\boldsymbol{F}$ contribute to $\boldsymbol{Q}$, Eq. (3) can be expressed using $\boldsymbol{F}$ and a distribution matrix $\boldsymbol{q}$

$$\boldsymbol{K}\boldsymbol{v} = \boldsymbol{q}\boldsymbol{F}. \tag{4}$$

For a system with n applied forces and n strain gauges, the relationship between them can be expressed by

$$\boldsymbol{\varepsilon} = \begin{bmatrix} \varepsilon_1 \\ \vdots \\ \varepsilon_n \end{bmatrix} = \begin{bmatrix} \boldsymbol{t}_1 \boldsymbol{T}_{\varepsilon_r 1} \widetilde{\boldsymbol{B}}_{e1} \boldsymbol{T}_{e1} \boldsymbol{N}_{e1} \\ \vdots \\ \boldsymbol{t}_n \boldsymbol{T}_{\varepsilon_r n} \widetilde{\boldsymbol{B}}_e n \boldsymbol{T}_{en} \boldsymbol{N}_{en} \end{bmatrix} \boldsymbol{L}\boldsymbol{K}^{-1}\boldsymbol{q}\boldsymbol{F} = \boldsymbol{S}^{-1}\boldsymbol{F}. \tag{5}$$

Solving this equation for the applied forces gives:

$$\boldsymbol{F} = \boldsymbol{S}\boldsymbol{\varepsilon}. \tag{6}$$

The matrix $\boldsymbol{S}$ is square due to the equal number of strain gauges and applied forces, and invertible if strain gauge locations are chosen correctly. Eq. (6) gives the basis for the inverse method. Depending on the model reduction used, $\boldsymbol{K}$ might not be invertible. The matrix $\boldsymbol{S}$ can then be found by introducing unit forces, and recording the strains

$$\boldsymbol{F}_1 = \begin{bmatrix} 1 \\ 0 \\ \vdots \\ 0 \end{bmatrix} \Rightarrow \boldsymbol{\varepsilon}_1, \qquad \boldsymbol{F}_2 = \begin{bmatrix} 0 \\ 1 \\ \vdots \\ 0 \end{bmatrix} \Rightarrow \boldsymbol{\varepsilon}_2, \quad \ldots \quad \boldsymbol{F}_n = \begin{bmatrix} 0 \\ \vdots \\ 0 \\ 1 \end{bmatrix} \Rightarrow \boldsymbol{\varepsilon}_n. \tag{7}$$

The recorded strains are the columns of the inverse compliance matrix $\boldsymbol{S}^{-1}$

$$\boldsymbol{S}^{-1} = [\boldsymbol{\varepsilon}_1 \quad \boldsymbol{\varepsilon}_2 \quad \ldots \quad \boldsymbol{\varepsilon}_n]_{n \times n}. \tag{8}$$

2.3. Mechanisms

Problems with the relations above arise when considering multibody mechanisms, because large displacements will be induced by actuators. If strain gauges and applied forces are located on the same component, and the forces are defined in the component local coordinate system, only gravitational effects need to be accounted for. On the other hand, if they are spread across different components, the compliance matrix becomes a function of actuator values $\boldsymbol{a}$ (lengths and angles)

$$\boldsymbol{S} = \boldsymbol{S}(\boldsymbol{a}). \tag{9}$$

Large displacements will also cause changes in strain readings due to gravitational forces. These need to be accounted for when using the measured strains in Eq. (6)

$$\boldsymbol{F} = \boldsymbol{S}(\boldsymbol{a})(\boldsymbol{\varepsilon} - \boldsymbol{A}(\boldsymbol{a})), \tag{10}$$

where $\boldsymbol{A}(\boldsymbol{a})$ is a vector function of actuator values representing strains caused by changes in gravitational forces from the position where the strain gauges were zeroed. Internal dynamic effects may also contribute to strain readings, as well as high frequency measurement noise. These effects can be removed by means of a low-pass filter, eliminating frequencies above the highest frequency of the applied load.

2.4. Cable and pulley system

The effect of a cable and pulley system can be added to the method by considering static force equilibrium at the end pulley (see Fig. 1). Three mutually perpendicular forces representing the reaction forces of the pulley are used as $\boldsymbol{F}$, and the equilibrium equations give the cable tension. This cable tension F_c is applied to the digital twin as forces on each pulley and the attachment point of the cable. The effect of these forces on strain gauge readings must also be accounted for when calculating the forces. This is done in a similar manner as for gravitational forces in Eq. (10), using a vector function $\boldsymbol{W}(\boldsymbol{a})$.

2.5. Drifting sensitivity

Measurements tend to be prone to drifting (low frequency) and signal noise (high frequency). Both causing deviation from the desired measurement value. While signal noise can be effectively removed by a low-pass filter, the drifting can have frequencies coinciding with load frequencies, and thus can be difficult to filter out. When forces are calculated from a drifted sensor signal with the proposed inverse method, the drift will be read as actual deformation; the method has no way of distinguishing it from the actual

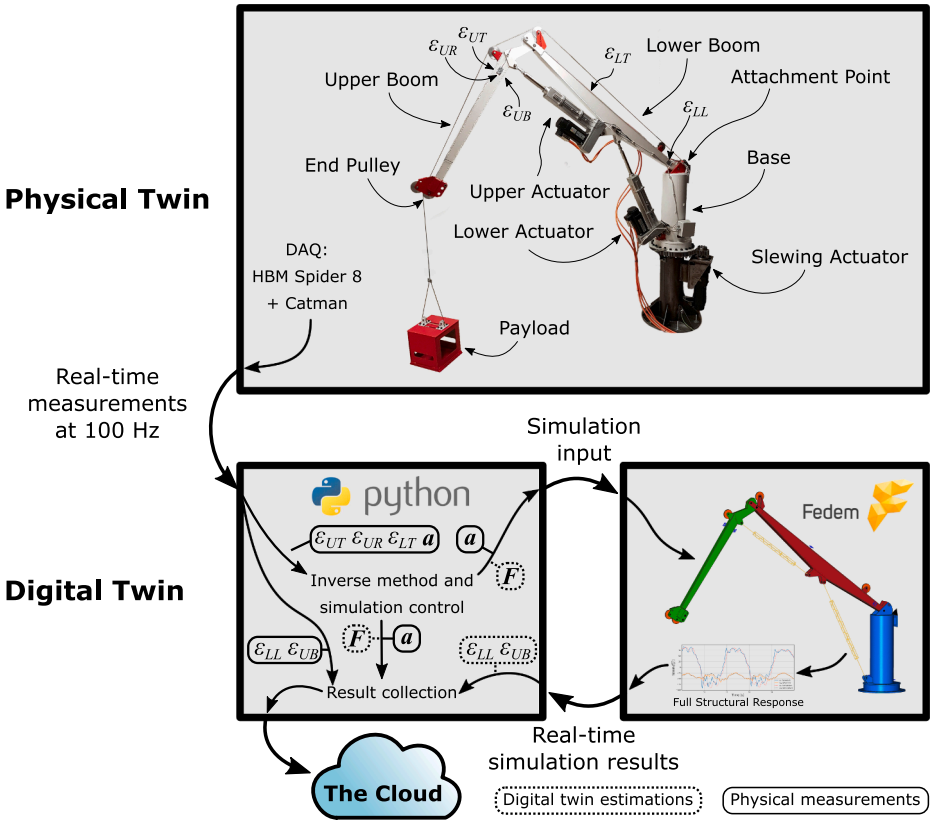

Fig. 1. Overview of the digital twin solution. The position of strain gauges are marked as ε_{ij}. The figure also shows the flow of data from the physical twin to the digital and finally to the cloud.

deformation. Thus, we get artificial forces that the physical twin was not subjected to.

The effect could be reduced by compensating for the drifting, e.g. compensating for temperature changes. However, if the setup used is very sensitive to drifting, meaning a very small drift causes large artificial forces, this might not be sufficient. An effort should therefore be made to minimize the effect of drifting. For comparing different setups, we can define a sensitiveness index s as

$$s = \|\boldsymbol{S}\boldsymbol{\varepsilon}_{drift}\|, \tag{11}$$

where $\boldsymbol{\varepsilon}_{drift}$ is some typical vector of drifted signal values, and the physical interpretation of s being the total resulting artificial force. The sensitiveness thus depends on $\boldsymbol{S}$. By optimizing the sensor distribution, s can be minimized.

3. Implementation

The digital twin was implemented using Fedem, a nonlinear finite element software made for fast digital twin computations, utilizing efficient CMS model reduction techniques [33]. Fedem also embeds efficient virtual strain gauge calculations enabling automated setup of the inverse method for any model. The inverse method itself was implemented in a Python script, which received sensor data, estimated forces and controlled the real-time simulation.

The physical and digital twin setup is given in Fig. 1. The payload was hanging in a cable running over pulleys to the base of the crane. Strain gauges ε_{UT}, ε_{UR} and ε_{LT} were used for Eq. (10) to estimate the forces. The forces on the end pulley were implemented as three mutually perpendicular forces in the upper boom local coordinate system. Two independent gauges ε_{UB} and ε_{LL} were used for validation.

3.1. Finite element model

The finite element models for each of the crane components were created with NX Nastran. 10-noded CTETRA elements were used for all parts [34]. The Fedem software imported the Nastran files, and connected the components by node to node connections. Rigid elements of type RBE2 were used at joints to facilitate this.

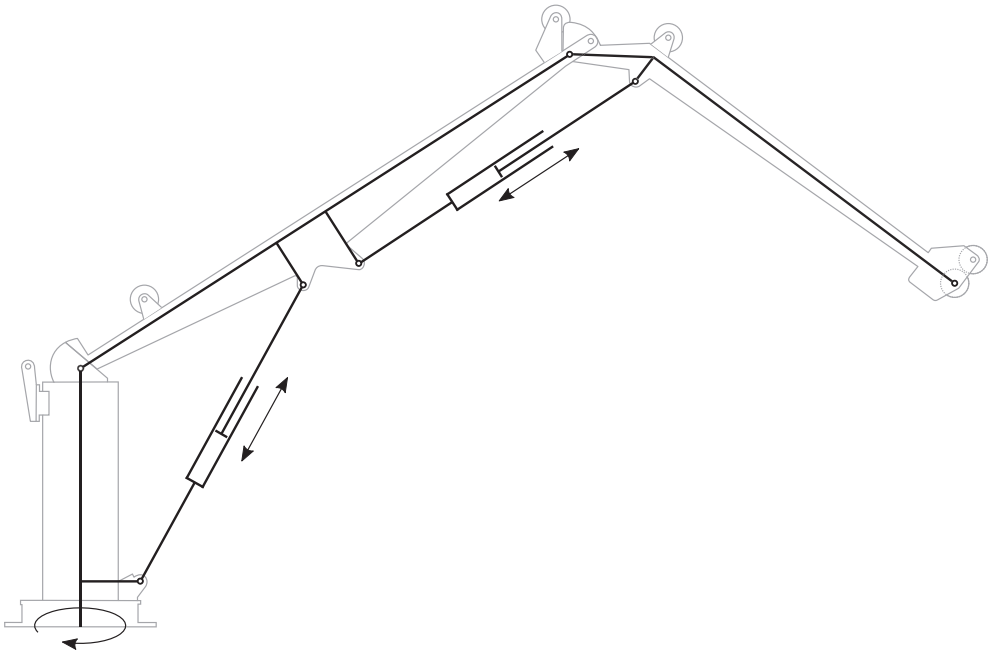

Fig. 2. Kinematic diagram of the crane, showing the degrees of freedom. The two linear actuators allow in-plane movement, while the rotating slewing actuator at the base rotates the crane into three dimensions.

3.2. Actuators

A kinematic diagram of the crane showing the actuators is shown in Fig. 2. As can be seen, the motion of the crane and payload is spatial, and not restricted to a linear or planar motion. Encoders on the actuator motors were used to record the motion of the crane. Their digital twin counterparts were modeled using an approach very similar to the penalty spring constraint method. The slewing actuator was modeled as a revolute joint with high rotational stiffness, and controlled by introducing a stress-free angle change. The joint was connected to the base and ground, which meant that the stress-free angle change forced the whole crane model to rotate.

The lower and upper actuators were modeled as linear springs and dampers. A stress-free length change was used to control the length of each actuator. The stiffness was chosen to be $1.0 \times 10^8 \frac{\mathrm{N}}{\mathrm{m}}$ for both actuators. This is approximately equivalent to the stiffness of the ball screw inside the physical actuators. With no damping, the stiff spring elements exhibit unwanted vibrations. The damping coefficient was found iteratively by comparing measurements and simulation results to be $2.0 \times 10^7 \frac{\mathrm{N\,s}}{\mathrm{m}}$. The mass of the actuators was added as concentrated masses at the spring end points. The mass of the side drive, motor and fixed cylinder was added to the lower end node, and the mass of the moving piston was added to the upper end node.

3.3. Strain rosettes

Virtual strain rosettes are implemented in Fedem with the formulation described in Section 2.2. A visualization of such a rosette is shown in Fig. 3b. The zero-stiffness membrane element is connected to four nodes in the same location as the physical rosette shown in Fig. 3a. If the type of the virtual rosette is set correctly, and the directions matched with the physical gauge, they become true twins. Filtering of the measured strains was achieved through a digital Butterworth low-pass filter. A cutoff frequency of 6 Hz and filter order 6 gave the best results. This filtering was applied only when using the measurements for force estimation, and thus the measurements shown as results are unfiltered.

The distribution of strain gauges proved to be important. The sensitivity index s was used to evaluate different distributions. A typical drifting observed in the physical measurements was $1 \frac{\mu\mathrm{m}}{\mathrm{m}}$ across all gauges. This was most likely due to small temperature changes, as no efforts were made to counter this effect. If strain gauges ε_{UT}, ε_{UR} and ε_{UB} were used, it resulted in a sensitivity index $s = 121.7$ N. Such an artificial force is very high, considering that a typical payload was 220 N. Replacing ε_{UB} with ε_{LT} however, reduced the sensitiveness to $s = 6.8$ N. The sensitiveness of the compliance matrix could potentially be improved even further by altering sensor placements, but for the purpose of this paper, the combination of ε_{UT}, ε_{UR} and ε_{LT} was satisfactory.

3.4. Lookup tables

Some matrices used in the proposed inverse method are dependent on actuator values when considering mechanisms. By choosing an appropriate number of points in the range of each actuator where the inverse method matrices $\boldsymbol{S}$ and $\boldsymbol{A}$ are to be calculated, a hyperdimensional array of matrices was constructed (the number of dimensions depending on the number of actuators).

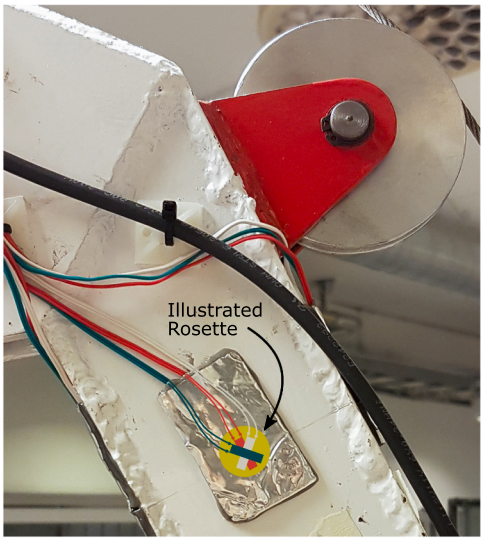

(a) A physical strain rosette with an illustrative overlay.

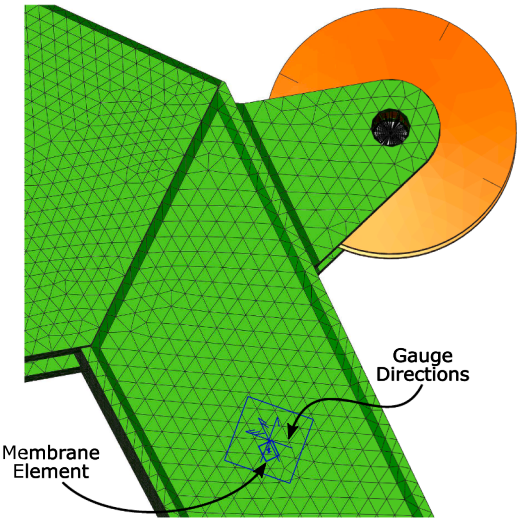

(b) A virtual strain rosette.

Fig. 3. A strain rosette ε_{UR} on the physical and digital twins. The physical rosette is covered by a protective substance, but is illustrated with overlaid graphics.

In simple terms, each entry to a matrix or vector was saved as a lookup table. This is illustrated in Fig. 4 for an $n \times n$ compliance matrix with two actuators. Actuator 1 has k interpolation points, while actuator 2 has m points. The value of any S_{ij} can be approximated by linear interpolation in the table to the right in the figure. Any number of actuators can be added by increasing the number of dimensions of the lookup table.

The calculation itself was automated by iterating through all possible combinations of interpolations points of the actuators and calculating the required matrices in each position. The entries of the gravitational force compensation matrix $\boldsymbol{A}$ were found from strain readings at zero load for the given position. The compliance matrix $\boldsymbol{S}$ was found by the method give by Eqs. (7) and (8) using unit forces. Finally, the cable force compensation matrix $\boldsymbol{W}$ was found in a similar manner through applying unit cable forces, though no matrix inversion was necessary. The required number of interpolation points depends on the nonlinearity of the matrices. For the crane, five interpolation points for each of the two linear actuators proved to be sufficient.

4. Results and discussion

Several tests were performed in order to benchmark the digital twin solution, and two representative runs with different payloads are presented in this paper. Each run started by lifting the payload with the crane, manually inducing abrupt movement in all three actuators to initiate spatial payload sway, and then finished by lowering the payload back to the ground. The actuator movement for each run in shown in Fig. 5.

The supplementary video shows a real-time simulation of the crane, with some result plots.

The accuracy of the inverse method and model was evaluated in two ways. First, the independent strain gauge measurements were used for the verification and evaluation of accuracy of the virtual strain gauges. Second, the estimated cable tension was compared to an expected static tension (no payload movement). Figs. 6a and 7 show these results from the run with the heaviest payload ($m = 32.2$ kg). In the strain measurement comparison there is good correlation between strain measurements, but the digital twin had some trouble replicating high frequency oscillations. This was expected as the inverse method assumes quazi-static behaviour. Some offset in mean values was also observed, and can most likely be attributed to measurement drifting due to e.g.

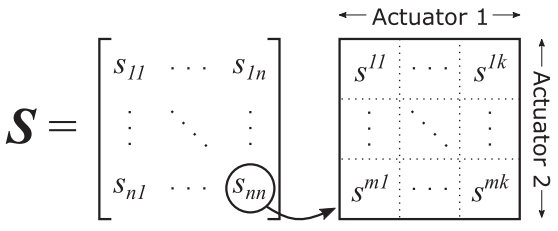

Fig. 4. A compliance matrix with two actuators as a hyperdimensional array. Each entry in the matrix (left) is a lookup table (right).

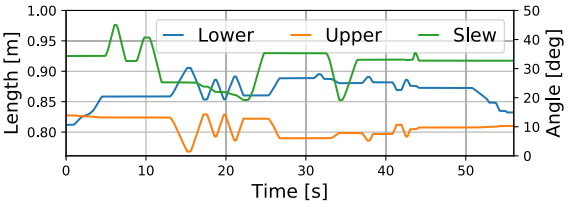

(a) 32.2 kg payload run.

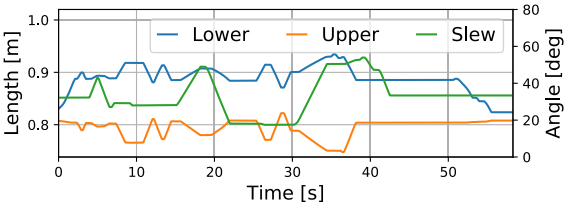

(b) 13.5 kg payload run.

Fig. 5. Measured actuator lengths for the lower and upper actuators, and an angle of the slewing actuator.

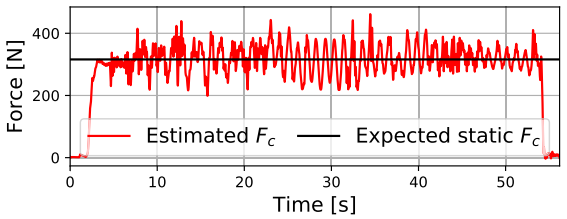

(a) Estimated cable tension and expected static tension.

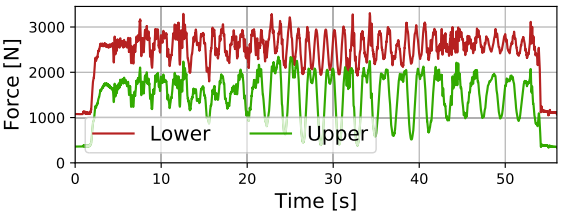

(b) Axial forces in actuators.

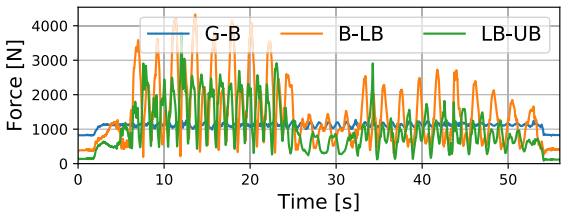

(c) Total joint forces.

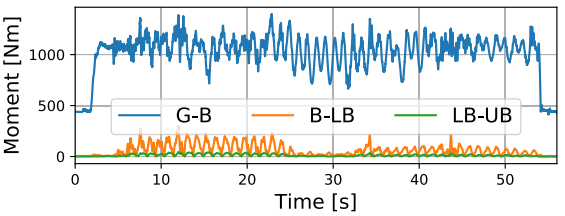

(d) Total joint moments.

Fig. 6. Force results from the run with 32.2 kg payload. Large oscillations in the estimated tension are caused by payload sway, and thus only the mean value of these oscillations should be compared to the expected static tension. Letters G, B, LB and UB indicate joints between ground, base, lower boom and upper boom.

temperature changes.

Looking at the force plot in Fig. 6a, large oscillations can be observed. This is due to inertia forces from the sway of the payload, and thus only the mean value of these oscillations should be compared to the expected static F_c. The effect of sensor drifting in strain measurements is apparent here also, with some low frequency variations in mean F_c.

Though inertia forces are included for the payload in the inverse method, the inertia forces of the crane itself is not. The Fedem software includes inertia forces of the crane components in the simulation, but the strain caused by this measured on the physical twin will be falsely converted to equivalent payload forces by the inverse method. The authors did not consider this to be a significant source of error in this particular case, but if the inertia forces in a different case are significant, they should be compensated for.

In order to evaluate if the results are sufficiently accurate, their use case must be considered. If the strain gauge measurements are used for fatigue damage calculations, a peak valley extraction is usually performed to reduce the number of data points. In this process, oscillations with an amplitude below a specified gate value are ignored. These small oscillations are considered to have no effect on the fatigue of the component. Such a processing of data for the independent gauge ε_{LL} is shown in Fig. 7c. It is clear that the inaccurate representation of high frequency oscillations does not affect the accuracy of fatigue damage calculations when data is processed in this manner.

In fact, the strain results from the digital twin can produce more accurate input for fatigue damage calculations. In the results of this paper, both the strain gauge measurements and simulation results are zeroed at the start of each run, but the crane components will actually be pre-strained due to the cranes own weight, giving a higher mean strain. While this pre-strain can be hard to identify using physical measurements on an assembled crane, they can be found easily with the digital twin by zeroing the virtual strain gauges before applying gravitational load to the simulation.

Some additional results of interest for condition monitoring are shown in Fig. 6b–d. These are all quantities that could be hard to measure, at least without modifications to the crane. Joint forces and moments are shown as totals for each joint, but are available as individual components in global or local coordinate systems as well.

Fig. 8 shows the main results from the run with the lighter payload (m = 13.5 kg). Here we observe a more pronounced effect of

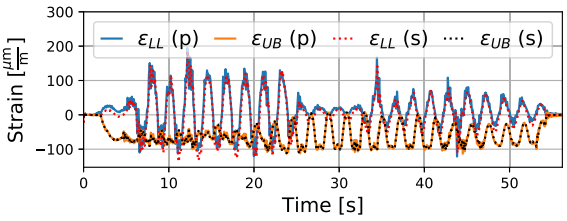

(a) Full time history.

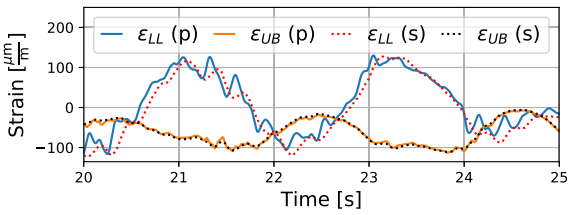

(b) Detail view.

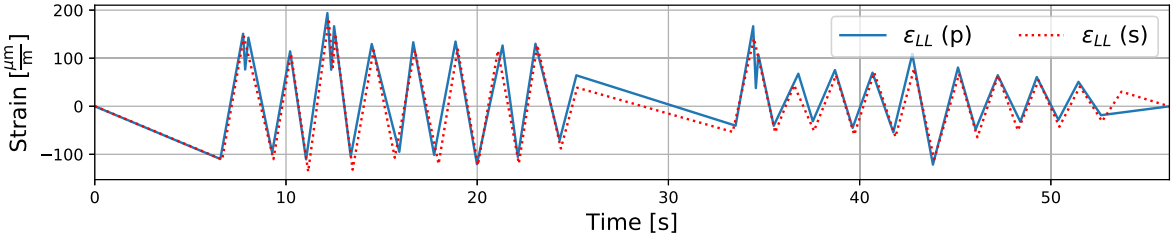

(c) Peak valley extracted strain history, with 30 $\frac{\mu m}{m}$ gate value.

Fig. 7. Independent strain gauge comparison for the run with 32.2 kg payload. Physical measurements and simulation results are marked with (p) and (s), respectively.

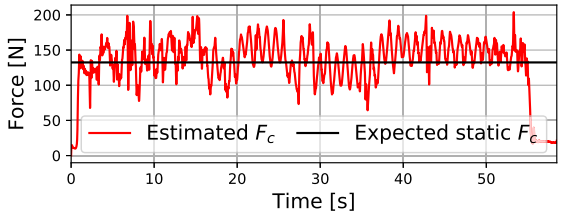

(a) Estimated cable tension and expected static tension.

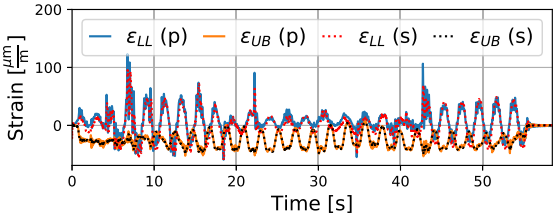

(b) Full time history.

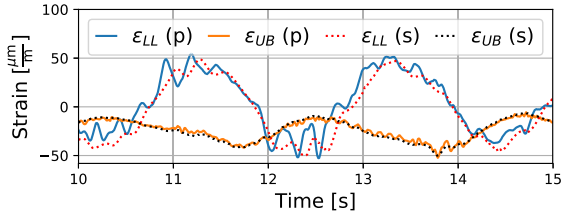

(c) Detail view.

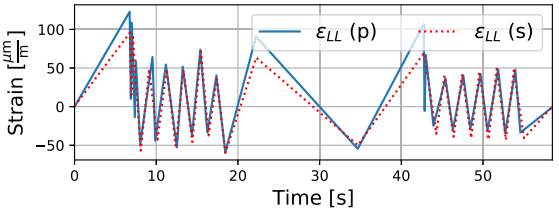

(d) Peak valley extracted strain history, with 30 $\frac{\mu m}{m}$ gate value.

Fig. 8. Main results for the run with 13.5 kg payload. Nomenclature and comments from Figs. 6 and 7 apply.

sensor drifting in both the force and strain plots. This can be explained by the fact that the magnitude of the strain signal is lower when using a lighter payload, making the drifting relatively larger compared to the actual signal. Thus, if higher accuracy at this load level is required, efforts should be made to compensate for the sensor drifting.

4.1. Error estimates

Quantifying the error between physical and virtual strain gauges is not straightforward. A simple time step by time step comparison would yield an unreasonable error due to the small offsets in time between the twins. Since mainly peak values are of interest for structural monitoring, these were chosen as basis for the error calculation. These could be paired between physical and virtual gauges, and thus removing the time offset problem. However, the number of peaks between the physical and virtual gauges were not the same. This was due to edge cases close to the gate value in the peak valley extraction, where the peak in one twin is barely

Table 1
Error results for cable tension and strain measurements. A gate value of 30 $\frac{\mu m}{m}$ was used for all cases, except for ε_{UB} with 13.5 kg payload where a lower value of 20 $\frac{\mu m}{m}$ had to be used due to low amplitude of the measurements.

Payload [kg]	δ_F [%]	**Gauge**	$\overline{\varepsilon_p}$ [$\frac{\mu m}{m}$]	δ_m [%]	δ_a [%]
32.2	1.4	ε_{LL}	90.6	15.0	7.5
		ε_{UB}	54.7	3.6	6.2
13.5	6.7	ε_{LL}	51.8	16.8	13.5
		ε_{UB}	26.2	6.1	6.0

included while the other is not. Therefore, peaks where a pair between physical and virtual measurements could not be found within 0.5 s time difference were ignored.

Depending on the use case of the digital twin, different measures of error would be of interest. If crane overload is to be monitored, then the magnitude of the strain is of interest. Since the value of a peak could potentially be zero, giving a division error, a mean absolute percentage error in relation to the mean absolute value was used for strain magnitude error:

$$\delta_m = \frac{1}{n}\sum_{t=1}^{n}\left|\frac{\varepsilon_{p,t} - \varepsilon_{s,t}}{\overline{\varepsilon_p}}\right| \times 100\% \tag{12}$$

Where δ_m is average magnitude percentage error, n is the number of measurements and $\varepsilon_{p,t}$ and $\varepsilon_{s,t}$ are the physical and virtual strain measurements for a given pair. $\overline{\varepsilon_p}$ denotes the mean absolute value of the physical measured strain peaks.

Overloading can also be monitored by the cable tension. The error was calculated by comparing the mean estimated cable tension $\overline{F_c}$ between 5 s and 50 s, where the payload was fully lifted, to the expected static tension mg:

$$\delta_F = \frac{\overline{F_c} - mg}{mg} \times 100\% \tag{13}$$

If the measurements are used for fatigue monitoring, the strain amplitude is the most important. The error in amplitude, δ_a, was evaluated by comparing strain difference between peaks:

$$\delta_a = \frac{1}{n-1}\sum_{t=1}^{n-1}\left|\frac{(\varepsilon_{p,t+1} - \varepsilon_{p,t}) - (\varepsilon_{s,t+1} - \varepsilon_{s,t})}{(\varepsilon_{p,t+1} - \varepsilon_{p,t})}\right| \times 100\% \tag{14}$$

The error results are displayed in Table 1. In general, the run with the heavier payload measured the least error. Strain gauge ε_{UB} was the most accurate, which is expected since it is located close to the gauges used in the inverse method. ε_{LL}, located further away, showed larger errors. In relation to the proposed sources of error, the equivalent temperature difference of the strain magnitude errors were between 0.14 °C and 1.36 °C (assuming a thermal expansion coefficient of $10 \times 10^{-6}\,\frac{1}{°C}$). It should also be noted that the error calculated with this procedure may be highly dependent on the chosen gate value, depending on the data.

5. Conclusion

In this work we presented an implementation of a digital twin with an inverse method using strain gauges as load sensors. A formulation for virtual strain gauges was used to find a linear relation between applied forces and measured strains. This relation provided the basis for an efficient nonlinear method suitable for digital twins with large displacements.

Experiments were conducted using a small-scale knuckle boom crane. A payload was lifted with a cable and moved to induce sway. Three strain gauges and encoders on the actuators provided the required input data for the digital twin. Two independent strain gauges were used to benchmark the accuracy of the digital twin solution.

The physical measurements showed good correlation with simulated strain time histories proving that both the crane model and inverse method are accurate. Cable tension was estimated within 1.4–6.7% of expected static tension, strain peak magnitude within 1.6–16.8% and strain amplitude within 6.0–13.5% of physical measurements, depending on payload weight and strain gauge location. This means that virtual sensor outputs from anywhere on the crane model can provide strain and load time histories for structural monitoring and fatigue damage estimation without further physical instrumentation.

Declaration of competing interest

The authors declare that they have no known competing financial interests or personal relationships that could have appeared to influence the work reported in this paper.

Acknowledgment

This work was partially funded by the Norwegian Research Council, SFI Offshore Mechatronics, project number 237896. The authors have also received support from SAP Norway Engineering Center of Excellence.

Appendix A. Supplementary material

Supplementary data associated with this article can be found, in the online version, at https://doi.org/10.1016/j.engfailanal.2020.104517.

References

[1] S. Haag, R. Anderl, Digital twin–proof of concept, Manuf. Lett. 15 (2018) 64–66.
[2] S. Boschert, R. Rosen, Digital twin—the simulation aspect, Mechatronic Futures, Springer, 2016, pp. 59–74.
[3] E. Negri, L. Fumagalli, M. Macchi, A review of the roles of digital twin in cps-based production systems, Procedia Manuf. 11 (2017) 939–948.
[4] D. Guivarch, E. Mermoz, Y. Marino, M. Sartor, Creation of helicopter dynamic systems digital twin using multibody simulations, CIRP Annals. (2019).
[5] E.J. Tuegel, A.R. Ingraffea, T.G. Eason, S.M. Spottswood, Reengineering aircraft structural life prediction using a digital twin, Int. J. Aerospace Eng. (2011).
[6] C. Li, S. Mahadevan, Y. Ling, S. Choze, L. Wang, Dynamic bayesian network for aircraft wing health monitoring digital twin, Aiaa J. 55 (3) (2017) 930–941.
[7] B.R. Seshadri, T. Krishnamurthy, Structural health management of damaged aircraft structures using digital twin concept, in: 25th AIAA/AHS Adaptive Structures Conference, 2017, p. 1675.
[8] Y. Cai, B. Starly, P. Cohen, Y.-S. Lee, Sensor data and information fusion to construct digital-twins virtual machine tools for cyber-physical manufacturing, Procedia Manuf. 10 (2017) 1031–1042.
[9] D. Botkina, M. Hedlind, B. Olsson, J. Henser, T. Lundholm, Digital twin of a cutting tool, Procedia CIRP 72 (2018) 215–218.
[10] W. Luo, T. Hu, C. Zhang, Y. Wei, Digital twin for cnc machine tool: modeling and using strategy, J. Ambient Intell. Humanized Comput. 10 (3) (2019) 1129–1140.
[11] C. Deng, R. Guo, P. Zheng, C. Liu, X. Xu, R.Y. Zhong, From open cnc systems to cyber-physical machine tools: a case study, Procedia CIRP 72 (2018) 1270–1276.
[12] R. Rosen, G. Von Wichert, G. Lo, K.D. Bettenhausen, About the importance of autonomy and digital twins for the future of manufacturing, IFAC-PapersOnLine 48 (3) (2015) 567–572.
[13] M. Schluse, M. Priggemeyer, L. Atorf, J. Rossmann, Experimentable digital twins—streamlining simulation-based systems engineering for industry 4.0, IEEE Trans. Industr. Inf. 14 (4) (2018) 1722–1731.
[14] F. Biesinger, D. Meike, B. Kraß, M. Weyrich, A digital twin for production planning based on cyber-physical systems: A case study for a cyber-physical system-based creation of a digital twin, Procedia CIRP 79 (2019) 355–360.
[15] R. Vrabic, J.A. Erkoyuncu, P. Butala, R. Roy, et al., Digital twins: Understanding the added value of integrated models for through-life engineering services, Procedia Manuf. 16 (2018) 139–146.
[16] Y. Zheng, S. Yang, H. Cheng, An application framework of digital twin and its case study, J. Ambient Intell. Humanized Comput. 10 (3) (2019) 1141–1153.
[17] T. Moi, A. Cibicik, T. Rølvåg, Digital twin based fatigue monitoring of a knuckle boom crane, published at 3rd International Conference on Structural Integrity and Durability (6 2019).
[18] T. Uhl, The inverse identification problem and its technical application, Arch. Appl. Mech. 77 (5) (2007) 325–337, https://doi.org/10.1007/s00419-006-0086-9.
[19] K. Liu, S. Law, X. Zhu, Y. Xia, Explicit form of an implicit method for inverse force identification, J. Sound Vib. 333 (3) (2014) 730–744, https://doi.org/10.1016/j.jsv.2013.09.040 URL http://www.sciencedirect.com/science/article/pii/S0022460X13008225.
[20] V. Jayalakshmi, K. Lakshmi, A.R.M. Rao, Dynamic force reconstruction techniques from incomplete measurements, J. Vib. Control 24 (22) (2018) 5321–5344, https://doi.org/10.1177/1077546317752709.
[21] Q. Li, Q. Lu, Time domain force identification based on adaptive lq regularization, J. Vib. Control 24 (23) (2018) 5610–5626, https://doi.org/10.1177/1077546318761968.
[22] Q. Li, Q. Lu, A revised time domain force identification method based on bayesian formulation, Int. J. Numer. Meth. Eng. 118 (7) (2019) 411–431, https://doi.org/10.1002/nme.6019.
[23] J. Sanchez, Observer-based force reconstruction technique, Ph.D. thesis Graduate School-New Brunswick, 2015.
[24] X. Li, H. Zhao, Z. Chen, Q. Wang, J. an Chen, D. Duan, Force identification based on a comprehensive approach combining taylor formula and acceleration transmissibility, Inverse Probl. Sci. Eng. 26 (11) (2018) 1612–1632, https://doi.org/10.1080/17415977.2017.1417407.
[25] K.-V. Yuen, K. Huang, Real-time substructural identification by boundary force modeling, Struc. Control Health Monit. 25 (5) (2018) e2151, https://doi.org/10.1002/stc.2151.
[26] T. Lai, T.-H. Yi, H.-N. Li, Parametric study on sequential deconvolution for force identification, J. Sound Vib. 377 (2016). https://doi.org/10.1016/j.jsv.2016.05.013.
[27] T. Zhu, S. ne Xiao, G. wu Yang, Force identification in time domain based on dynamic programming, Appl. Math. Comput. 235 (2014) 226–234, https://doi.org/10.1016/j.amc.2014.03.008.
[28] Z. Li, Z. Feng, F. Chu, A load identification method based on wavelet multi-resolution analysis, J. Sound Vib. 333 (2) (2014) 381–391, https://doi.org/10.1016/j.jsv.2013.09.026 URL http://www.sciencedirect.com/science/article/pii/S0022460X13007803.
[29] J. Liu, X. Han, C. Jiang, H.M. Ning, Y.C. Bai, Dynamic load identification for uncertain structures baed on interval analysis and regularization method, Int. J. Comput. Methods 08 (2011). https://doi.org/10.1142/S0219876211002757.
[30] Q. Li, Q. Lu, Force localization and reconstruction using a two-step iterative approach, J. Vib. Control 24 (17) (2018) 3830–3841, https://doi.org/10.1177/1077546317713366.
[31] J. Liu, X. Sun, X. Han, C. Jiang, D. Yu, A novel computational inverse technique for load identification using the shape function method of moving least square fitting, Comput. Struct. 144 (2014) 127–137.
[32] T. Rølvåg, B. Haugen, M. Bella, F. Berto, Fatigue analysis of high performance race engines, published at 3rd International Conference on Structural Integrity and Durability (6 2019).
[33] T. Rølvåg, M. Bella, Dynamic test bench for motocross engines, Adv. Mech. Eng. 9 (2017), https://doi.org/10.1177/1687814017726921 168781401772692.
[34] Siemens Industry Software, Element Library Reference (2014). URL https://docs.plm.automation.siemens.com/data_services/resources/nxnastran/10/help/en_US/tdocExt/pdf/element.pdf.